Science Advances
AAAS

advances.sciencemag.org/cgi/content/full/6/36/eabb6500/DC1

Supplementary Materials for

Anisotropic ultrasensitive $PdTe_2$-based phototransistor for room-temperature long-wavelength detection

Cheng Guo, Yibin Hu, Gang Chen, Dacheng Wei, Libo Zhang, Zhiqingzi Chen, Wanlong Guo, Huang Xu, Chia-Nung Kuo, Chin Shan Lue, Xiangyan Bo, Xiangang Wan, Lin Wang*, Antonio Politano*, Xiaoshuang Chen*, Wei Lu

*Corresponding author. Email: wanglin@mail.sitp.ac.cn (L.W.); antonio.politano@univaq.it (A.P.); xschen@mail.sitp.ac.cn (X.C.)

Published 2 September 2020, *Sci. Adv.* **6**, eabb6500 (2020)
DOI: 10.1126/sciadv.abb6500

This PDF file includes:

Supplementary Materials

1. Materials characterization

The structure of the grown crystals was examined by X-ray diffraction (Bruker D2 PHASER) using Cu K α radiation and Laue diffraction (Photonic Science) at room temperature is shown in Fig. S1a. The strong (00n) peaks of $PdTe_2$ can clearly be seen, and no other impurity peaks can be found, indicating nice crystallization of the $PdTe_2$ sample. The clear spots in the Laue pattern (Fig. S1b) and low-energy electron diffraction (LEED) pattern (Fig. S1c) suggest a high quality nature of the single crystal. Only six diffraction spots exist in this LEED pattern, representing an almost commensurate (1 ×1) lattice with respect to the $PdTe_2$ surface. The Raman spectrum in Fig. S1d shows two peaks at ~74.7 and ~133.7 cm^{-1} respectively.

2. First-principles simulation

In structural relaxation using VASP, the atoms are fully relaxed until the maximum force becomes less than 0.01 $eVÅ^{-1}$, the lattice constant a is 4.1 Å and the lattice constant ratio c/a is 1.269. The atomic structure of $PdTe_2$ is following. The armchair, zigzag and c direction are represented by a, b, c respectively (Fig. 1a).The bandstructure of $PdTe_2$ is following (Fig. S1e). Individual Fermi surfaces of four bands crossing the Fermi level, projected onto the k_x−k_y plane (Fig. S1f). This result is consistent with other theoretical results[12].

3. Theoretical basis of photogalvanic effect and photon drag effect

Now we discuss the origin of the observed photocurrents, which are induced by spatially homogeneous terahertz radiation and scale with the second power of the radiation electric field. This approach allows us to explore what kind of photocurrents is allowed in the considered system and to describe their variation upon a change of the macroscopic parameters, such as radiation intensity, polarization, and incident angle[34]. With this, the response of the charge carriers ensemble to the external field can be characterized conveniently by the coordinate- and time-dependent electric current density $\boldsymbol{j}$ ($\boldsymbol{r}$,t). It is expanded in a power series in the external alternating electric field $\boldsymbol{E}$($\boldsymbol{r}$,t) in the form of a plane wave:

$$\boldsymbol{E}(\boldsymbol{r},t) = \boldsymbol{E}(\omega,\boldsymbol{q})e^{-i\omega t+i\boldsymbol{qr}} + \boldsymbol{E}^{*}(\omega,\boldsymbol{q})\boldsymbol{e}^{i\omega t-i\boldsymbol{qr}} \quad (1)$$

Where $\omega = 2\pi f$ is the angular frequency and $\boldsymbol{q}$ is its wave vector. Limiting the consideration to the second-order effects, we obtain the photocurrent density $j \propto \boldsymbol{J}$ in the form. In our work, we focus discuss on linear photogalvanic effect and photon drag effect in Dirac semimetal $PdTe_2$. By general symmetry arguments it can be shown that the linear photogalvanic effect (LPGE) and photon drag effect (PDE) photocurrents are given by

$$j_\lambda = \sum_{\mu\nu} \chi_{\lambda\mu\nu} \left(E_\mu E_\nu^* + E_\nu E_\mu^*\right)/2 + \sum_{\delta\mu\nu} T_{\lambda\delta\mu\nu}\, q_\delta E_\mu E_\nu^* \quad (2)$$

Where $\chi_{\lambda\mu\nu}$ and $T_{\lambda\delta\mu\nu}$ are components of a third-rank and a fourth-rank tensor, respectively, and q_δ is the wave vector of the radiation in the sample.

The first term on the right-hand side of equation (2) is called the LPGE because it is independent of the sign of the circular polarization and is usually measured using linearly polarized radiation. The second term represents the PDE, which yields a current due to momentum transfer from photons to electrons.

The LPGE arises in homogeneous samples under homogeneous excitation due to an asymmetry of the scattering of free carriers on phonons, static defects, or other carriers in noncentrosymmetric media. Microscopically, the LPGE current consists of a so-called ballistic contribution and a shift contribution. The PDE arises due to a momentum transfer from photons to free carriers. The PDE described by the second term of the right-hand side of equation (2) is mediated by a fourth-rank tensor T. Therefore there is no symmetry restriction for this effect.

As shown by equation (2), the LPGE current is linked to the symmetrized product $E_\mu E_\nu^*$ by a third-rank tensor $\chi_{\lambda\mu\nu}$ which in turn is symmetric in the last two indices. Therefore $\chi_{\lambda\mu\nu}$ is isomorphic to the piezoelectric tensor and may have non-zero components in media lacking a centre of symmetry. Equation (2) can be simplified considering the point group C_{3v}, which describes the symmetry of the surface states in $PdTe_2$. Taking into account the fact that we detected only photocurrents excited by

linearly polarized radiation that are even in normal incidence, we can omit all contributions of photocurrents sensitive to the radiation helicity. Under these conditions we derive for *j*

$$j_x = \chi\left(E_x^2 - E_y^2\right) - Tq_y E_y E_z \quad (3)$$

$$j_y = -2\chi E_x E_y - Tq_y E_x E_z \quad (4)$$

The constants χ and *T* are coefficients describing the LPGE and PDE, respectively. LPGE has the polarization dependence and varies with the angle θ according to $j_x \propto (E_x^2 - E_y^2)$. PDE has the polarization dependence and varies with the angle θ according to $j_x \propto E_y E_z$.

4. Measurement of low temperature photocurrent

In addition to the room temperature measurement of $PdTe_2$ device in the text, we also did the photocurrent measurement related to low temperature. As shown in Figure S2, the photocurrent increases as the temperature decreases at different voltages. In particular, the relationship between the photocurrent and the responsivity with the change of voltage was compared respectively at 300 K and 77 K. It can be seen that the device has higher photocurrent and responsivity at low temperature. At 50 mV, the responsivity of 77 K is twice that of 300K. If experimental conditions permit, it may be possible to combine the superconducting characteristics of $PdTe_2$ to achieve ultra-high responsivity at low temperature.

5. Experimental proof and theoretical calculation of anisotropy photocurrent effect

To substantiate anisotropy photocurrent effect on $PdTe_2$, dozens of devices have been fabricated with the same structure and measured under the same condition, all of which exhibit similar behavior with good stability and repeatability at zero-bias. More data on devices are provided in Fig. S3. The fluctuation of the photocurrent response may be ushered in the variation of layer thickness, orientation of crystallographic axis. To elucidate the anisotropy of the second order nonlinearity of photogalvanic effect, a crossed-contacted four-electrode device is measured at first. Fig.S4-a shows the

resistance in the x and y directions differ by no more than 4%, indicate the anisotropy of photocurrent is not caused by the difference of resistance in different directions. The same results can be replicated in other devices (Fig.S4-b). The reproducibility of the experiment proves the anisotropy photocurrent effect on $PdTe_2$ experimentally. The in-plane anisotropy is found to be signified near the Dirac node following the asymmetric bandstructures. Using DFT calculation along with the nonequilibrium Green's function formalism[32,] we can enumerate qualitatively the PGE photocurrent when the $PdTe_2$ devices are irradiated by linear polarized light (Fig.S4-c). It reveals the essential involvement of the anisotropy harnessed by the PGE photocurrent during the experimental processes.

6. Polarization modulated photogalvanic effect

To verify further the rectified current under polarization modulated applied field as well as anisotropy, circular-contacted device is also studied. Measurement diagram as described in the Fig.4a. The IV characterizations of the $PdTe_2$ device with circle-electrode shown in Fig.S4-d indicate the contact quality is basically the same at circle-electrode. The difference in photocurrent is not caused by different contact quality. In compared with the incident field, the electric field will be redistributed as caused by both the oscillating current among the electrode pattern and the incident polarization. The redistributed electric field can be simulated by FDTD method. A phase difference between E_x and E_y will be introduced, so that the photocurrent changing versus incident polarization will not only have a 2θ term of linear polarization, but also have a component of 4θ term. The observed the inversion and symmetry of photocurrent collected between nearest electrode pairs can be used to distinguish PGE and photothermal effect (PTE). PTE is depending on the asymmetry of power intensity distribution between adjacent electrodes ($|E|^2$). It can be observed that the distribution of PGE on circle-electrode (Fig.S5), indicate the symmetry relationship between $PdTe_2$ devices with circle-electrode and polarization. PTE photocurrent varying with polarization can be obtained by the distribution of $|E|^2$ on circle-electrode as shown in Fig. S6. The polarization dependence of photocurrent exhibits a phase shift between

every two adjacent pairs of electrodes, and in the meantime, the photocurrent in every electrode pairs will change its sign when the polarization angle changes. The behavior of PTE photocurrent does not accord with the experimental results, which also indicates the leading mechanism of PGE. The same results can be observed in Fig.S7. The reproducibility of the experiment proves the correctness of our analysis.

7. Noise current as a function of frequency

The noise current of the $PdTe_2$ device is shown in Fig. S8. For NEP analysis, the noise power spectra were measured using amplifiers and then digitized with a dynamic signal analyzer-SR785. A cross correlation algorithm is used to average out the instrument noise. Just battery and ballast resistors were used to avoid extra noises due to external circuit. The device is kept in a shielded dark enclosure when experiment. The NEP is 1.3 $pW/Hz^{0.5}$ at 0.12 THz and 57 $pW/Hz^{0.5}$ at 0.3 THz, estimated by NEP = I_n/R_A, where I_n is the noise current in $A/Hz^{0.5}$, the resistance r=372 Ω. For evaluating NEP values, the noise current is extracted from the noise power spectra at frequency bandwidth of 1 KHz, and the responsivity are estimated at the same frequency.

8. Detection performance and THz imaging application

Under finite bias voltage, the signal-to-noise ratio of the device is improved without bringing any deterioration in response time. The response speed defined as time required for the rising from 10% to 90% (or analogously, falling from 90% to10%) is determined to be about 1.3 μs (or 2.5 μs).

Our device is already exploitable for high-resolution terahertz transmission imaging. The terahertz source is tuned to 0.12 THz and 0.3 THz operated at room temperature. As a test object, two-dimensional raster scanning imaging is devoted to single-pixel detector, with total 200×200 points acquired by lock-in technique, a test object is fixed at focal plane of x-y axis and the transmitted power can been recorded by two-dimensional translation with the photodetector operating in zero bias and 20 ms integral time. The obtained imaging results are shown in Figure 5h and 5i.

9. Measurement of photocurrent on grapheme-$PdTe_2$ heterojunction

As we know, $PdTe_2$ is a semimetal material, so its resistance is very low and it has a high dark current as a photodetector. Based on this, we also fabricated graphene-$PdTe_2$ heterojunction to suppress dark current, as shown in Figure S9-a. Graphene-$PdTe_2$ heterojunction device has large resistance (Figure S9(b-c)), and a large photocurrent in the range of 0.04 THz to 0.3 THz (Figure S9-d). As an excellent terahertz detector material and a van der Waals material, heterogeneous junction device based on $PdTe_2$ is expected to achieve better detection performance at future.

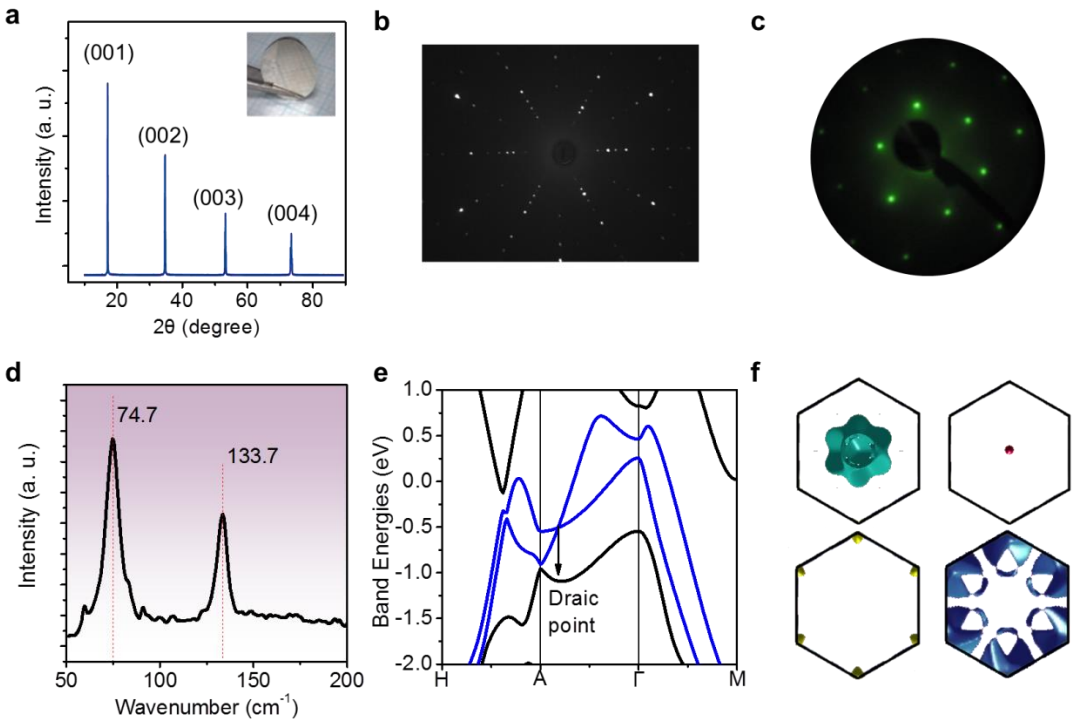

Fig. S1. **Materials characterization and band structure of $PdTe_2$.** (a) The x-ray-diffraction data of the $PdTe_2$. (b) The Laue pattern of $PdTe_2$. (c) low-energy electron diffraction pattern of the $PdTe_2$ crystal. (d) Raman spectrum of the $PdTe_2$. (e) The band structure of $PdTe_2$. (f) Individual Fermi surfaces of four bands crossing the Fermi level, projected onto the k_x−k_y plane.

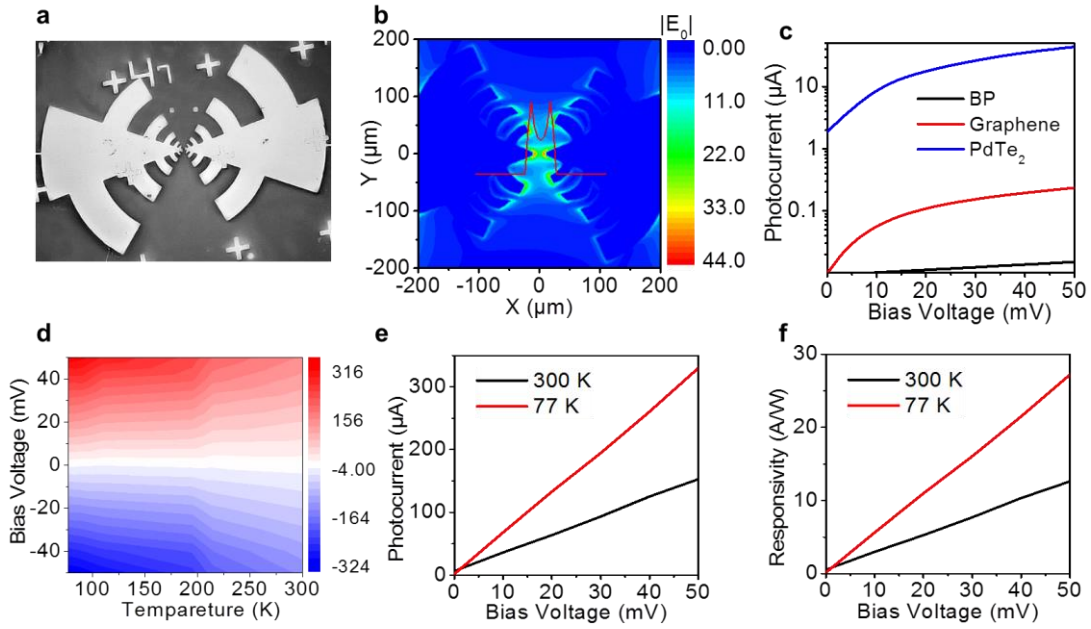

Fig. S2. **Supplementary measurements for $PdTe_2$ devices.** (a) The SEM of $PdTe_2$-based device. The same metal contact and antenna structure that produce symmetrical electric fields are used to eliminate the PTE. (b)The distribution of electric field $|E_0|$ at $PdTe_2$-based device. (c) The photocurrent of $PdTe_2$ was compared with that of other materials. (d) Temperature dependent photocurrent distribution. The photocurrent (e) and responsivity (f) are varied with bias voltage at 300 K and 77 K.

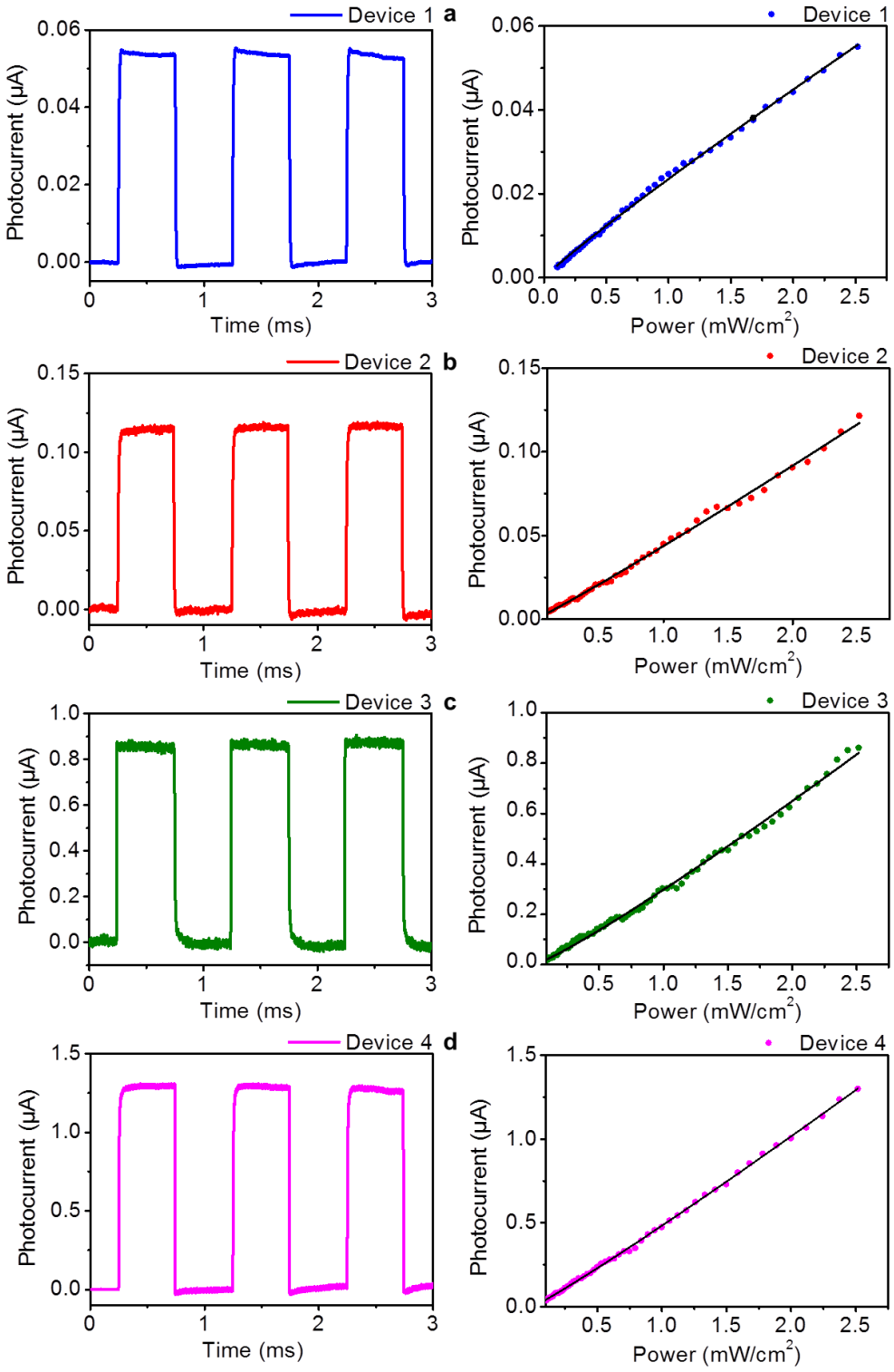

Fig. S3. **The photocurrent of $PdTe_2$-based devices.** The photocurrent response under 1 KHz modulation frequency (left) and dependence of the radiation power intensity (right) of (a-d) Device 1-4.

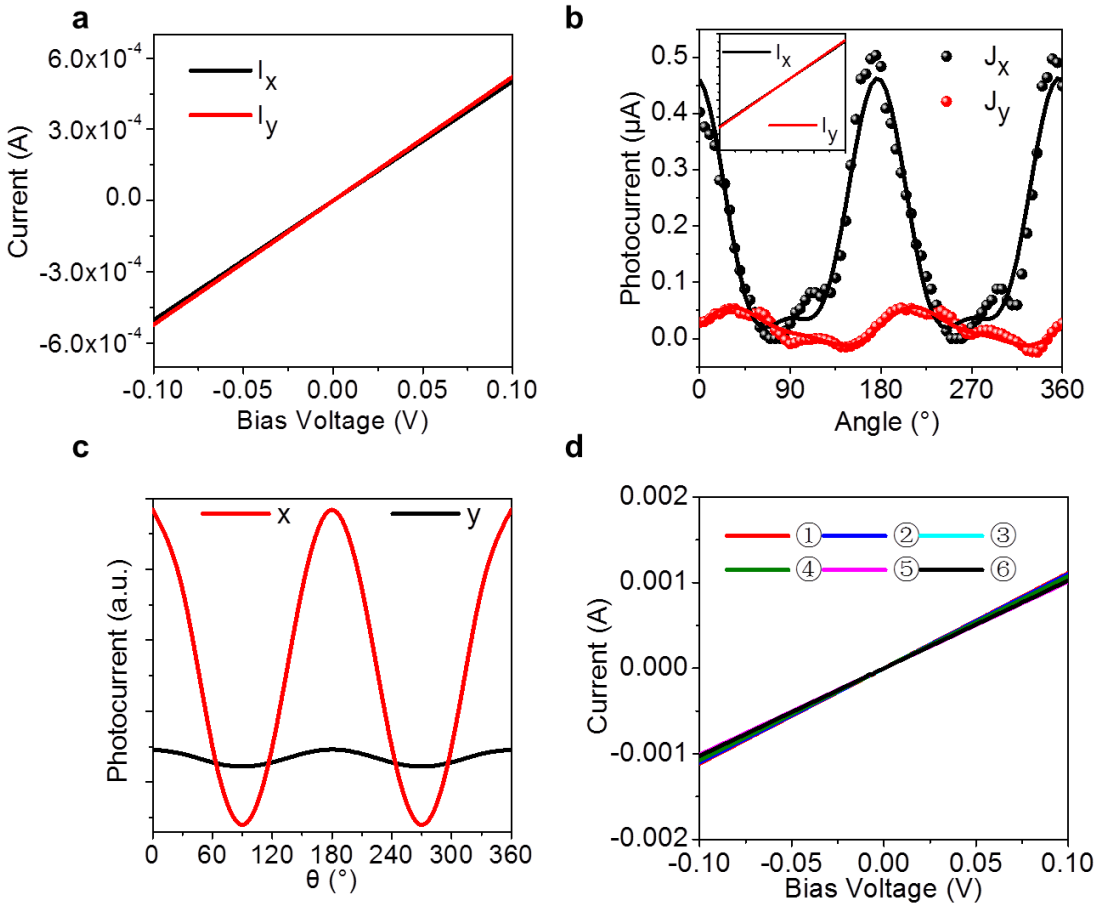

Fig. S4. **The IV characterization of the $PdTe_2$ devices.** (a) The IV characterization of the $PdTe_2$ device at Fig. 3. (b) The photocurrent and IV characterization of another $PdTe_2$ devices in the x and y directions. (c) Using DFT calculation enumerates qualitatively the PGE photocurrent of $PdTe_2$ device. (d) The IV characterization of the $PdTe_2$ devices with circle-electrode.

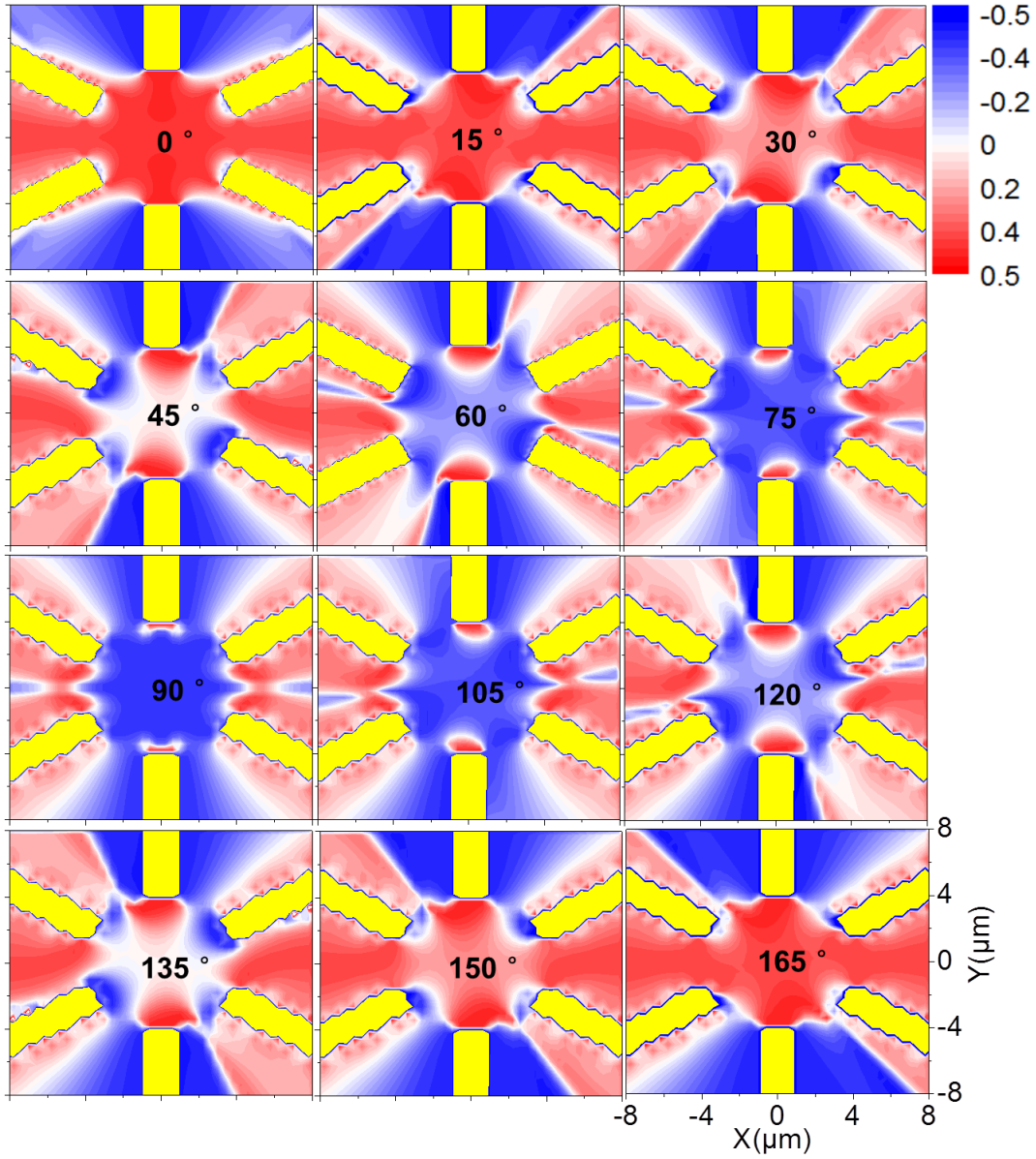

Fig. S5. The PGE of the $PdTe_2$ devices with circle-electrode depend on the polarization.

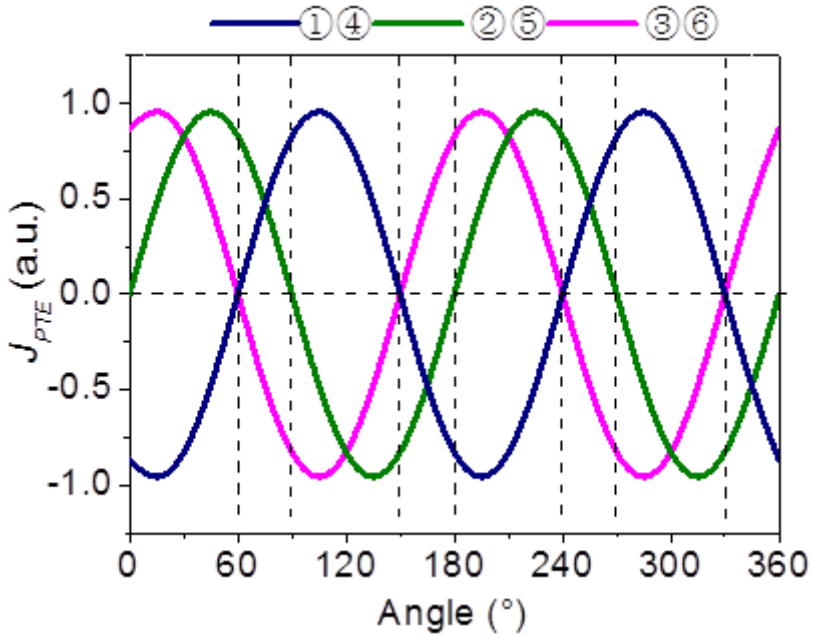

Fig. S6. The J_{PTE} of the $PdTe_2$ devices with circle-electrode depend on the polarization.

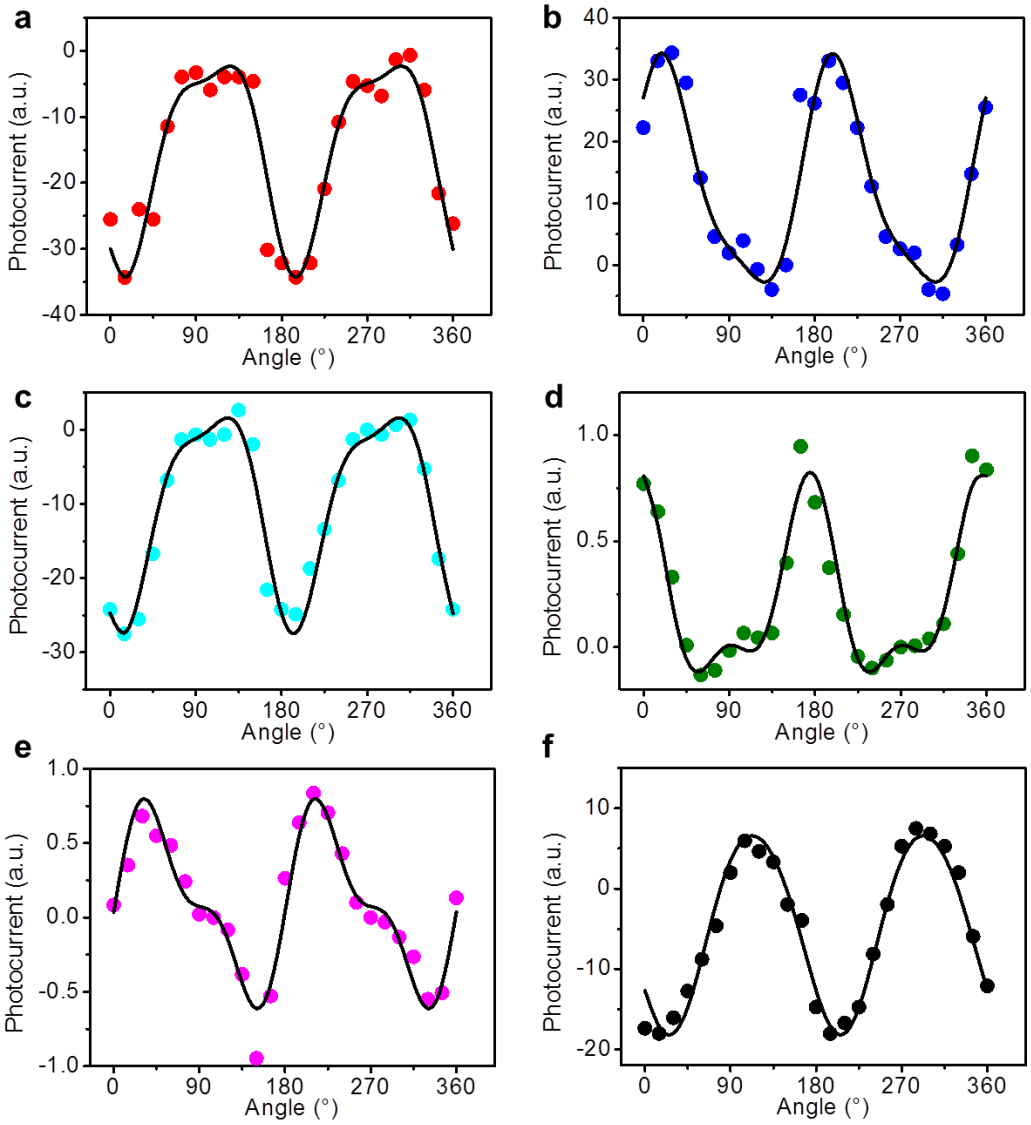

Fig. S7. **Polarized-depended photocurrent of another $PdTe_2$ device.** (a)-(f) The dependence of the photocurrent of ①~⑥ on polarization angle.

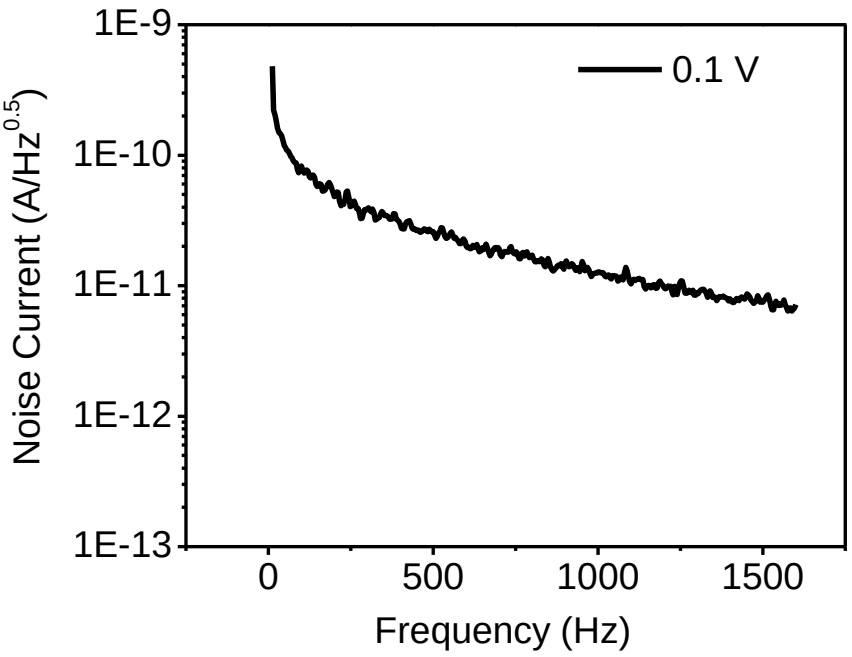

Fig. S8. Noise current as a function of frequency for the $PdTe_2$ device at external bias 0.1 V.

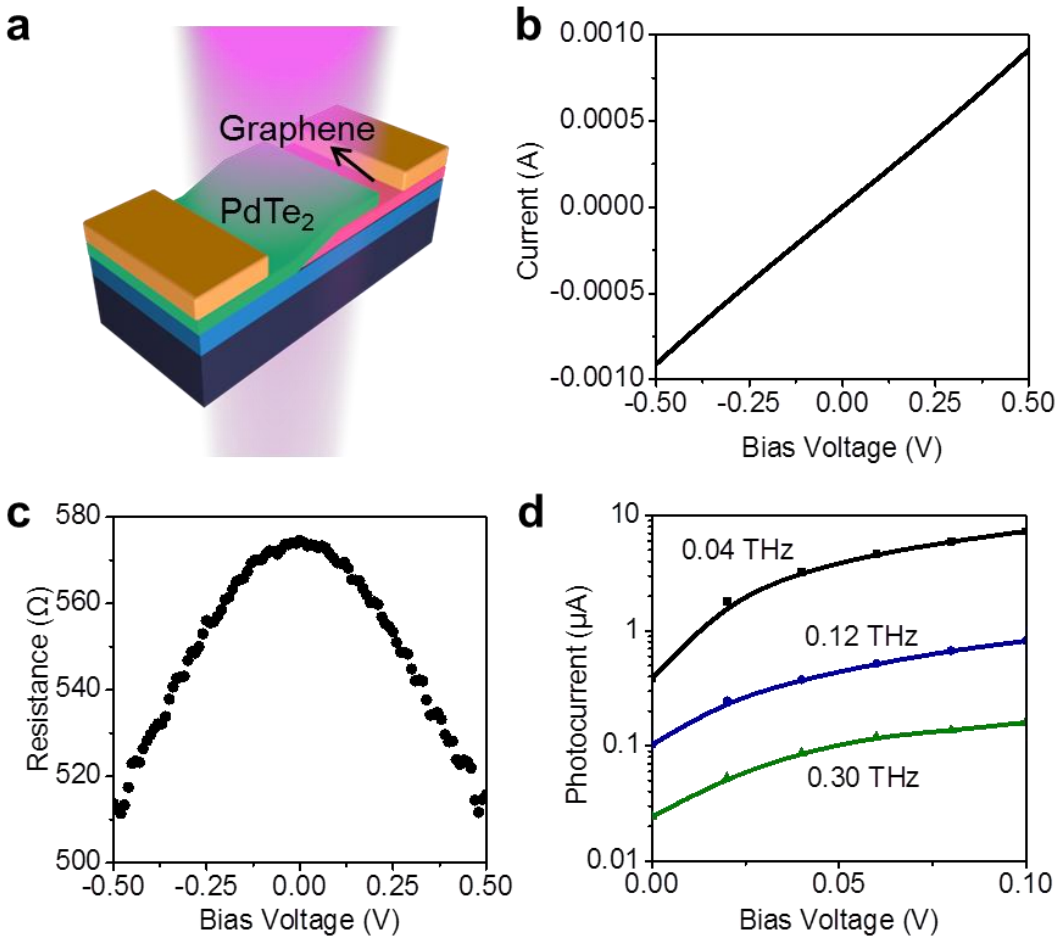

Fig. S9. **Graphene-$PdTe_2$ heterojunction.** (a) Schematic diagram of graphene-$PdTe_2$ heterojunction. IV (b), resistance (c) and photocurrent (d) of graphene-$PdTe_2$ device.

Table S1. Parameters for some THz photodetectors.

Description	Responsivity/NEP	Spectral range	Devise type	Reference
$PdTe_2$	>1.5 $pW/Hz^{0.5}$	0.04THz-0.3THz	PGE	Our work
Graphene	>34 $pW/Hz^{0.5}$	0.05-0.45THz	Ballistic rectifier	(*29*)
TI	>10 $nW/Hz^{0.5}$	0.29-0.33THz	Plasma	(*30*)
BP	>40 $nW/Hz^{0.5}$	0.26-0.38THz	Plasma	(*31*)

TI=Topological insulators, BP= Black Phosphorus.